PAPER

Facile fabrication of hierarchical $ZnCo_2O_4$/NiO core/shell nanowire arrays with improved lithium-ion battery performance†

Zhipeng Sun,[ab] Wei Ai,[a] Jilei Liu,[a] Xiaoying Qi,[c] Yanlong Wang,[a] Jianhui Zhu,[a] Hua Zhang[c] and Ting Yu*[ade]

We report a facile and controllable strategy for the fabrication of three-dimensional (3D) $ZnCo_2O_4$/NiO core/shell nanowire arrays (ZCO/NiO NWs) on nickel (Ni) foam substrates by a simple, cost-effective, two-step, solution-based method. Ultra-thin NiO nanosheets are revealed to grow uniformly on the porous $ZnCo_2O_4$ nanowires with many interparticle mesopores, resulting in the formation of 3D core/shell nanowire arrays with hierarchical architecture. In comparison with the pristine $ZnCo_2O_4$ nanowire arrays (ZCO NWs), the ZCO/NiO NWs exhibit significantly improved Li storage properties, in terms of higher capacity, enhanced rate capability and improved cycling stability when applied as binders and additive-free anode materials for lithium-ion batteries. The superior Li storage performance of the ZCO/NiO NWs could be attributed to the synergetic effect between the $ZnCo_2O_4$ core and the NiO shell, as well as its unique hierarchical architecture, which ensures a large specific surface area and good conductivity. Our results may offer very useful guidelines in scrupulously designing 3D core/shell nanowire-array electrodes using cheap, earth-abundant materials in energy storage applications.

Introduction

With an ever increasing list of promising applications, there is a surge in developing efficient and scalable strategies for fabricating nanostructures with diverse and tunable properties.[1–3] Recently, the growth of heterostructures with controllable dimensions has sparked great research interest, owing to the fact that diverse properties can be generated by tailoring the morphology, composition, and assembling organization of the primary nanobuilding blocks.[4–6] Most current research work has been focused on freestanding core/shell nanowire heterostructures due to their large surface areas, high surface-to-body ratios, more active surface sites, good ionic/electronic conductivities, as well as better permeabilities in nanoscale electronics, catalysis, chemical sensing, and energy storage applications.[7–15]

Particularly, for serving as electrode materials for LIBs[10–12] and supercapacitors,[13–15] tremendous efforts toward freestanding core/shell nanowire heterostructures have been witnessed. It has been found that heterostructured nanowire architecture can make use of the advantages of both components and offer special properties through a reinforcement or modification of each other.[13] For instance, the high performance of SnO_2/V_2O_5 core/shell nanowires as LIB electrodes was obtained owing to the synergetic effect exerted by SnO_2 and V_2O_5 as well as the unique core/shell structure.[16] Moreover, Co_3O_4/TiO_2 core/shell nanowires as LIB anodes also present high reversible capacity, improved cycling stability and excellent rate capability, compared with the pristine TiO_2, which is due to the synergistic effect of both the component and short diffusion length of the thin Co_3O_4 nanosheets.[17] Furthermore, ordered TiO_2/α-Fe_2O_3 core/shell nanowire arrays on carbon textiles as LIB anodes exhibit high rate capability and outstanding cycling performance.[11] Similarly, some core/shell nanowire or nanotube arrays, such as $WO_{3−X}$/$MoO_{3−X}$,[15] Co_3O_4/MnO_2,[18] $NiCo_2O_4$/MnO_2,[19] as electrode materials exhibit enhanced capacitive performances and excellent stabilities for supercapacitors. For these above applications, it is extremely desirable to fabricate freestanding core/shell nanowire heterostructures due to their enhanced physical and chemical properties as compared to the single components.[20] Significantly, the interface/chemical distributions are homogeneous at the nanoscale; thus, a fast ion and electron transfer is guaranteed.[10] Furthermore, they

[a]Division of Physics and Applied Physics, School of Physical and Mathematical Sciences, Nanyang Technological University, 637371, Singapore. E-mail: yuting@ntu.edu.sg

[b]Xinjiang Uygur Autonomous Region Product Quality Supervision and Inspection Institute, 830011, China

[c]School of Materials Science and Engineering, Nanyang Technological University, 63639798, Singapore

[d]Department of Physics, Faculty of Science, National University of Singapore, 117542, Singapore

[e]Graphene Research Centre, National University of Singapore, 117546, Singapore

† Electronic supplementary information (ESI) available. See DOI: 10.1039/c4nr00533c

generally provide a high surface area to increase the interfacial kinetics and porous texture to accommodate the stress relaxation and a direct pathway for electron transport.[3,6]

To date, for lithium storage, $ZnCo_2O_4$ and NiO have been considered as two kinds of anode materials superior to graphite because of their high theoretical capacity, low cost, and good environmental benignity.[21,22] However, the disadvantages of $ZnCo_2O_4$ and NiO are also apparent. In particular, the simple nanostructure, poor intrinsic conductivity and significant volume change of either $ZnCo_2O_4$ or NiO nanostructures during lithium insertion/deinsertion reaction will lead to the cracking of electrode films during subsequent electrical isolation and fast capacity fading. All these drawbacks unavoidably constitute a major obstacle for their practical application in LIBs.[23] To overcome the above-mentioned issues, efforts have been extensively focused toward the exploitation of different novel nanostructures (such as nanotubes, nanoplates and nanowires/rods) of $ZnCo_2O_4$ (ref. 24–26) and NiO.[27,28] Inspired by combining the unique properties of individual constituents, we envision fabricating the novel core/shell nanowire arrays, which can exhibit intriguing properties by taking advantage of 3D hierarchical structural features, nanometer-sized effects and good stability of the secondary nanostructure assemblies.[12] Therefore, it is also meaningful to investigate the potential application of 3D ZCO/NiO NWs as binders and additive-free anode materials in LIBs.

Herein, we demonstrate a freestanding 3D ZCO/NiO NWs fabricated by a simple, cost-effective hydrothermal growth, followed by chemical bath deposition methods, in which the surface of the $ZnCo_2O_4$ nanowire cores are enclosed by ultrathin NiO nanosheet shells (see Fig. 1). Fortunately, the 3D ZCO/NiO NWs hold several favourable merits, which are as follows: (1) both the hydrothermal synthesis and chemical bath deposition method have proven to be an effective, low-cost and applicable technique; (2) long ZCO NWs serve as both the backbone and conductive connection for the NiO nanosheets, which can obviously increase the robust hierarchical porosity and high surface area of the hybrid feature; (3) as a shell, ultrathin nanosheet-like NiO enlarges the interface area with electrolytes and protects the inner $ZnCo_2O_4$ backbone, which can boost the electrochemical reaction and improve durability; and (4) the ZCO/NiO NWs grown on Ni foam as LIB anodes may not need any ancillary additives such as carbon black and polymer binder. Due to these unique advantages of

freestanding core/shell nanowire arrays, the resulting hierarchical ZCO/NiO NWs exhibit higher capacity, enhanced rate capability and improved cycling stability, compared to pristine ZCO NWs, when applied as binders and additive-free anode materials for LIBs.

Experimental

Materials preparation

Synthesis of ZCO NWs on 3D Ni foam. In a typical process,[21] 0.2 mmol zinc nitrate ($Zn(NO_3)_2 \cdot 6H_2O$), 0.4 mmol cobalt nitrate ($Co(NO_3)_2 \cdot 6H_2O$), 0.4 mmol ammonium fluoride (NH_4F) and 1 mmol urea ($CO(NH_2)_2$) were added to a given amount (25 mL) of distilled water, and the resulting homogeneous solution was transferred into a Teflon-lined stainless-steel autoclave. After placing a piece of cleaned Ni foam substrate (2 cm × 4 cm), the autoclave was sealed and maintained at 120 °C for 5 h, and then cooled to room temperature. The samples were washed several times with deionized water and dried at 60 °C for 12 h in a vacuum oven. Finally, the ZCO NW samples with black colour were thermally treated at 400 °C for 2 h in a tube furnace.

Synthesis of ZCO/NiO NWs on 3D Ni foam. The as-prepared ZCO NW samples were used as the scaffold for NiO nanosheet growth by a facile chemical bath deposition (CBD). In a typical process,[29] solution for CBD was prepared by adding 2 mL of aqueous ammonia (25%) to the mixture of 10 mL of 1 M nickel sulfate and 8 mL of 0.25 M potassium persulfate in a 50 mL Pyrex beaker. Then, ZCO NWs were used as the growth substrate and placed vertically in the Pyrex beaker, which was shaken by a KS 130 Shakers (IKA) with the speed of 250 rpm. After immersion in the CBD solution for 1 h at room temperature, the substrate was removed and rinsed with an excess of distilled water and several times with ethanol. This substrate was then dried at 60 °C for 12 h in vacuum oven. Finally, the substrate was annealed at 300 °C for 1 h in a tube furnace to obtain the final product (brown colour).

Materials characterization

Powder X-ray diffraction (XRD) patterns were collected using an X-ray diffractometer with Cu Kα radiation ($\lambda = 1.5418$ Å). Scanning electron microscopy (SEM) images were obtained using a HITACHI S-4300 microscope. High-resolution transmission electron microscopy (HRTEM) observation and energy-dispersive X-ray spectroscopy (EDS) elemental mapping were carried out on a HRTEM JEM-2010FEF instrument. Nitrogen sorption analysis was performed on a Micromeritics (NOVA 4200e) analyzer at 77 K. The Brunauer–Emmett–Teller (BET) surface area was calculated from the linear part of the BET plot. The pore-size distribution was derived from the adsorption branch of the isotherm. Raman spectroscopy was performed using a WITEC CRM200 Raman system equipped with a 532 nm laser source and a 100× objective lens.

Electrochemical measurement

Sample-covered Ni foam was cut into round pieces (diameter ≈ 13 mm). A piece of the sample was used directly as the working
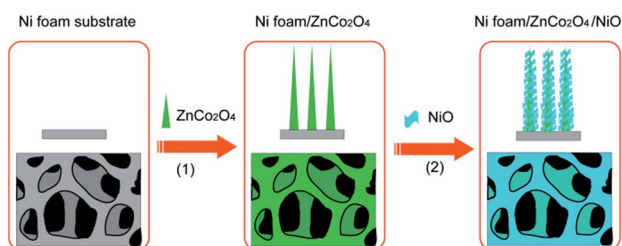

Fig. 1 Schematic illustration of the fabrication processes of ZCO/NiO NWs directly on the Ni foam substrate.

electrode without any polymeric binder or carbon black. The CR2016 coin-type cells were assembled in an Ar-filled glovebox (Mbraun, Unilab, Germany) by using ZCO/NiO (loading density $\approx$ 0.43 mg cm^{-2}) and ZCO (loading density $\approx$ 0.28 mg cm^{-2}) directly on the Ni foam as anode materials. A Li-metal circular foil (0.59 mm thick) was used as the counter and reference electrode, a microporous polypropylene membrane was used as the separator, and a 1.0 M solution of LiPF$_6$ in mixed ethylene carbonate (EC) and diethyl carbonate (DEC) (EC : DEC, 1 : 1 by volume) was used as the electrolyte. The cell was aged for 15 h before measurement. Cyclic voltammetry (CV, 0.01–3.0 V, 0.5 mV s^{-1}) was carried out on an electrochemical workstation (CHI 760D). Galvanostatic charging/discharging tests were performed on a NEWARE battery tester at different current rates with a voltage window of 0.01–3.0 V (*vs.* Li$^+$/Li). The electrochemical impedance spectroscopy (EIS) measurement was performed with the open-circle potential by applying an AC voltage of 5 mV over the frequency range from 100 kHz to 0.1 Hz.

Results and discussion

Our strategy for the fabrication of freestanding 3D ZCO/NiO NWs on a 3D Ni foam substrate followed the two-step process, which is schematically depicted in Fig. 1. Firstly, the self-assembled ZCO NWs are grown directly on the 3D Ni foam substrate. Then, the obtained ZCO NWs are uniformly aligned onto the Ni foam surfaces without secondary nanostructures (Fig. 2a and b). Close observation of the nanowires shows that the individual ZCO nanowire with an average diameter of 100 nm is porous (Fig. 2b, inset), which is obviously different from the precursor ZCO NWs because of annealing treatment (Fig. S1†). After the controllable deposition of NiO nanosheets on the surface of ZCO NWs by CBD, the nanostructures of core/shell NWs are formed. The top-view SEM images (Fig. 2c and d) illustrate that the as-prepared ZCO/NiO NWs are distributed uniformly and adhere firmly to the fuzzy foam surface of Ni with an average length of about 7.0 μm (Fig. S2†). Furthermore, close observation shows that the surfaces of the ZCO nanowire backbones are covered by highly dense secondary NiO nanosheets (Fig. 2e and f). These NiO nanosheets are closely connected with each other and form a networked structure (Fig. 2e). Moreover, the diameter of the individual core/shell ZCO/NiO nanowire is approximately 200 nm, and the average thickness of the secondary NiO nanosheets is about 6.4 nm (Fig. 2f). The growth mechanism of the core/shell nanowire heterostructures are the "oriented attachment" process and "self-assembly" process (also shown schematically in Fig. 1), which involves a spontaneous self-organization between the neighboring particles to share a common crystallographic orientation, followed by the joining of these particles at a planar interface. This process is particularly relevant in the nanocrystalline regime, in which bonding between the particles reduces the overall energy by removing surface energy associated with unsatisfied bonds.[3,13] In our experiments, the ZCO NWs act as the backbone to guide the preferential NiO deposition. In order to gain more insight into the evolutional process of hierarchical ZCO/NiO NWs, a series of time-dependent CBD processes for NiO growth are conducted. It
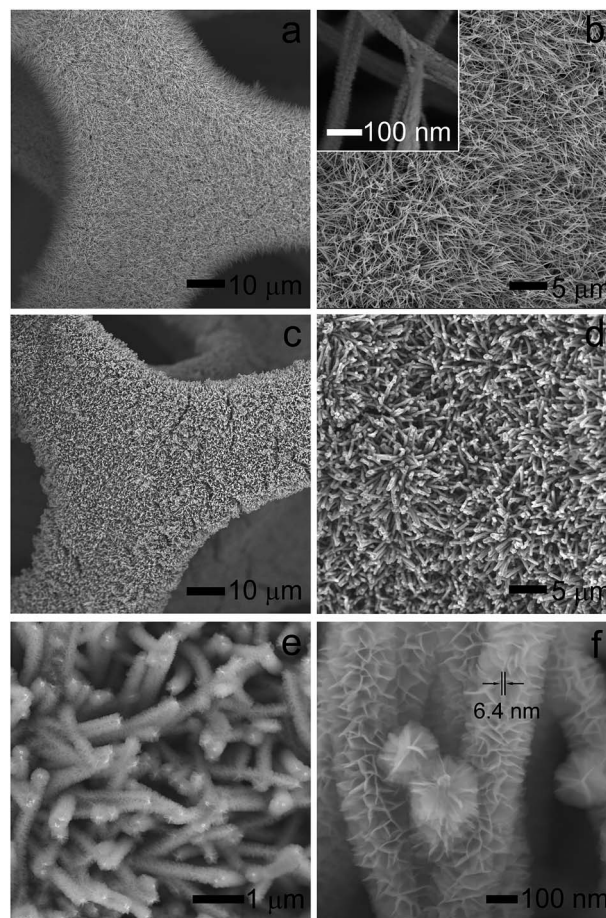

Fig. 2 SEM images of (a and b) ZCO NWs and (c–f) ZCO/NiO NWs grown on the 3D Ni foam substrate.

can be seen from the SEM images (Fig. S3†) that the ZCO/NiO NWs with different morphologies and nanostructures can be achieved in different stages of deposition times.

Detailed microstructures and compositions of the ZCO NWs and ZCO/NiO NWs were further investigated by TEM. It can be clearly observed that the ZCO nanowire is quite porous with an average diameter of around 100 nm and is composed of numerous nanoparticles of 8–21 nm in size (Fig. 3a and b). Moreover, the HRTEM image (Fig. 3b, inset) shows lattice fringes corresponding to an interplanar distance of ∼0.240 nm that can be attributed to the (311) plane of a ZnCo$_2$O$_4$ phase.[21,26] Compared with the pristine ZCO NWs, a portion of the hierarchical nanostructure of ZCO/NiO NWs shows that highly dense NiO nanosheets emanated from the surface of an individual ZCO nanowire (Fig. 3c, inset). Evidently, it can be clearly seen that secondary NiO nanosheets with many pores grow on the surface of the porous ZCO nanowire backbone. This indicates that the ZCO/NiO NWs may exhibit a highly reactive surface area, which will favour the electron transportation among the entire core/shell NW area. Moreover, the HRTEM image (Fig. 3c) taken from the shell region reveals that the lattice fringes with spacing of 0.209 nm and 0.239 nm are recognized, which corresponds to the (200) and (111) planar space of the cubic NiO, respectively.[22] Furthermore, the EDS mapping analysis of a
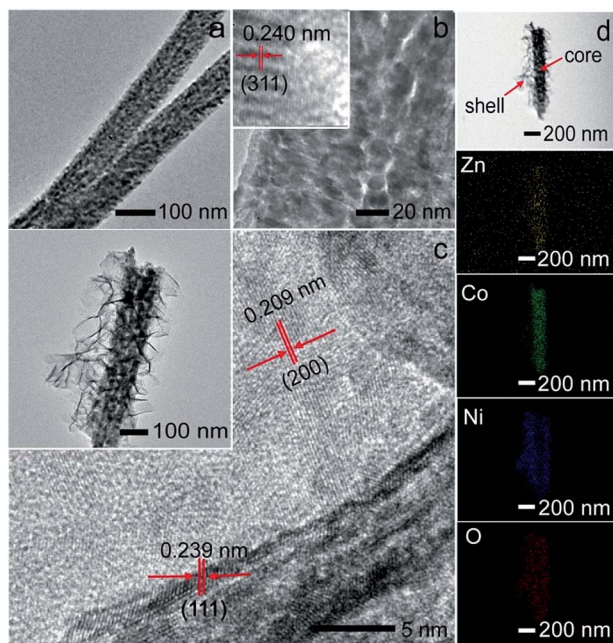
Fig. 3   (a and b) TEM images of ZCO nanowire (inset: lattice-resolved HRTEM image) and (c) TEM image (inset) and lattice-resolved HRTEM image of ZCO/NiO nanowire. (d) TEM image of a single ZCO/NiO nanowire and the corresponding TEM-EDS elemental mapping of Zn, Co, Ni, and O.

single ZCO/NiO nanowire also confirms the ZCO core/NiO shell hierarchical nanostructure, in which the Zn, Co, Ni and O signals appear to have similar shapes, as shown in corresponding TEM image (Fig. 3d and S4†). This indicates that an intriguing core/shell NWs nanostructure has been successfully fabricated. This conclusion can also be supported by the Raman and XRD results mentioned below. The existence of the NiO and ZCO in the as-prepared ZCO/NiO NWs is reflected in the Raman spectra (Fig. S5†).[30,31] The crystal phase of the ZCO NWs and ZCO/NiO NWs were analyzed by XRD measurement (Fig. S6†). All of the diffraction peaks in the XRD pattern of the ZCO NWs can be indexed to the spinel $ZnCo_2O_4$ phase (JCPDS card no. 23-1390).[21] Moreover, the two peaks located at 43.2° and 62.5° match well with the (200) and (220) planes of cubic NiO[29] (JCPDS card no. 4-0835), as evidenced from the XRD pattern of the ZCO/NiO NWs. These results definitely confirm that the adopted synthesis strategy successfully achieves ZCO/NiO NW nanostructures that integrate the ZCO nanowires and NiO nanosheets. In addition, the porosity and specific surface area of the ZCO NWs and ZCO/NiO NWs were further investigated, as shown in Fig. S7.† It is clearly shown that the pore-size distribution of ZCO NWs is within 5–20 nm, whereas the pore-size distribution of ZCO/NiO NWs is around 2–5 nm after the bare ZCO NWs were coated with the NiO nanosheets. Furthermore, the ZCO/NiO NWs also exhibit a high specific surface area of 119.9 m^2 g^{-1}, which is almost 1.4 times larger than that of the ZCO NWs (85.1 m^2 g^{-1}). This indicates that ZCO/NiO NWs possess high hierarchical porosity, possibly due to numerous ultrathin NiO nanosheets with porous nanostructures coating the surface of the porous ZCO NWs.

To investigate the electrochemical performances of ZCO NWs and ZCO/NiO NWs, the as-obtained arrays were used directly as anodes for battery assembly without adding any binders or conductive additives. Fig. 4a shows the first three CV curves of the ZCO/NiO NW electrodes at a scan rate of 0.5 mV s^{-1}. In the first cathodic sweep, both the ZCO/NiO NWs and ZCO NWs (Fig. S8a†) exhibit a clear, irreversible reduction peak at about 0.5 V, which is attributed to the formation of the solid electrolyte interface (SEI) layer that was caused by reduction of the electrolyte and the irreversible reduction of $ZnCo_2O_4$ and NiO.[23,24,26,32] However, the reduction peak of ZCO NWs (Fig. S8†) shifts to a higher potential at 0.86 V in the subsequent discharge cycles, suggesting a different lithium-insertion reaction, which is in agreement with the previous reports.[21,32] Similarly, the reduction peak of ZCO/NiO NWs is replaced by two new peaks at 0.86 and 1.25 V after the first cycle. Compared with the CV curves of the ZCO NWs, the extra peak at 1.25 V can be ascribed to the decomposition of NiO. The significant difference in the CV curves between the first and subsequent cycles for the ZCO/NiO NWs indicates that it experiences an irreversible transition after the initial discharge process.[21] Moreover, in the anodic sweep, the two broad oxidation peaks located at 1.81 and 2.24 V correspond to the oxidation of Zn to Zn^{2+}, Co to Co^{3+}, and Ni to Ni^{2+}.[22,23] The above mentioned electrochemical processes of the as-obtained arrays are summarized as follows:[22,27,28]
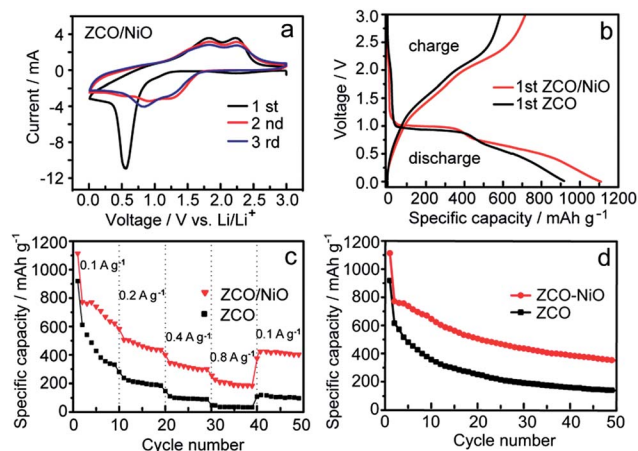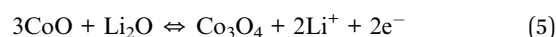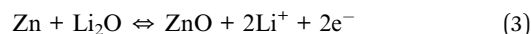
$$8Li^+ + ZnCo_2O_4 + 8e^- \Leftrightarrow 2Co + Zn + 4Li_2O \qquad (1)$$

$$xLi^+ + Zn + xe^- \Leftrightarrow Li_xZn \ (x \le 1) \qquad (2)$$

$$Zn + Li_2O \Leftrightarrow ZnO + 2Li^+ + 2e^- \qquad (3)$$

$$Co + Li_2O \Leftrightarrow CoO + 2Li^+ + 2e^- \qquad (4)$$

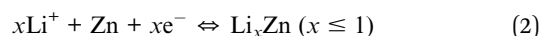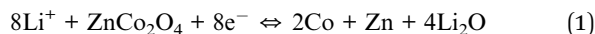$$3CoO + Li_2O \Leftrightarrow Co_3O_4 + 2Li^+ + 2e^- \qquad (5)$$

Fig. 4   (a) The first three CV curves of the ZCO/NiO NWs at a scanning rate of 0.5 mV s^{-1}. (b) The first discharge/charge profiles of the ZCO NWs and ZCO/NiO NWs at a current density of 0.1 A g^{-1}. (c) Rate capabilities of the ZCO NWs and ZCO/NiO NWs at various current densities. (d) Cycling performances of the ZCO NWs and ZCO/NiO NWs at a constant current density of 0.1 A g^{-1}.

$$NiO + 2Li^+ + 2e^- \Leftrightarrow Ni^0 + Li_2O \qquad (6)$$

$$Ni^0 + Li_2O \Leftrightarrow NiO + 2Li^+ + 2e^- \qquad (7)$$
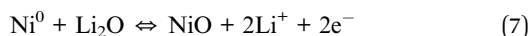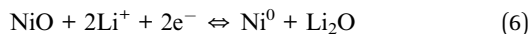
The first discharge (Li$^+$ insertion) and charge (Li$^+$ extraction) profiles of the ZCO/NiO NWs and ZCO NWs are illustrated in Fig. 4b. There is a wide, steady discharging plateau at ~1.0 V in the first cycle, followed by a gradual voltage decrease. Notably, the ZCO/NiO NWs exhibit an initial discharge capacity of 1116.4 mA h g^{-1}, which is higher than that of the ZCO NWs (919.2 mA h g^{-1}). Furthermore, the ZCO/NiO NWs also have a lower initial irreversible capacity loss of 30.5%, compared to 34.1% for ZCO NWs, which can be possibly attributed to the synergetic effect between the ZnCo$_2$O$_4$ and NiO, as well as its unique hierarchical architecture. Moreover, the irreversible capacity loss could be due to the solid electrolyte interphase (SEI) formation and the reduction of metal oxide to metal with Li$_2$O formation, which is commonly observed for a variety of electrode materials.[23] To gain further insight into the advantages of ZCO/NiO NWs for lithium storage, the rate and cycling performances of the ZCO NWs and ZCO/NiO NWs are also evaluated. Fig. 4c shows the rate performance of the arrays. It is notable that despite the severe capacity degradation in the first ten cycles, the ZCO/NiO NWs always deliver specific capacities two to three times higher than those of the ZCO NWs with the current density increasing from 0.2 A g^{-1} to 0.8 A g^{-1}. Moreover, with the current rate being lowered back to 0.1 A g^{-1}, both electrodes are able to recover to high capacity again. In addition, EIS measurements of the ZCO NW and ZCO/NiO NW electrodes are performed to probe the kinetic properties of the ZCO/NiO NWs, as shown in Fig. S8b.† Apparently, the resulting Nyquist plots exhibit two distinct parts: a semicircle in the high frequency region and a sloped line in the low frequency region. It should be noted that the diameter of the semicircle for the ZCO/NiO NWs (44.8 Ω) is apparently smaller than that of the ZCO NWs (62.8 Ω), whereas the contact resistances between the electrode materials and the electrolyte are similar, which suggest that the ZCO/NiO NWs possess low charge-transfer resistances. These results suggest that the NiO nanosheets shell coated on the ZCO NWs can not only enable much easier charge transfer at the electrode/electrolyte interface, compared with the ZCO NWs, but also can significantly enhance the electronic conductivity of the ZCO/NiO NWs during the cycling processes.[22] Additionally, Fig. 4d depicts the cycling performance of both samples up to 50 cycles. It demonstrates a significant drop in the capacity of second cycle for the two electrodes due to the initial irreversible loss. Despite the relatively faster capacity-fading behaviour, the ZCO/NiO NWs show much larger capacity and significantly improved cycling stability compared to the pristine ZCO NWs. For example, the capacities of the 50th cycle are found to be 357 mA h g^{-1} and 152 mA h g^{-1} for the ZCO/NiO NW and ZCO NWs electrodes, respectively. The above results provide sufficient evidence about the enhancement of the composite materials over the single ones, although the enhancement is not simply a result of the introduction of a higher-capacity component.[3,10] Instead, the enhancement more likely originates from the unique nanostructure of the composite electrode. The improved performance of the ZCO/NiO NWs can be attributed to the unique hierarchical nanostructures of the ZCO/NiO NWs, which can be elaborated as follows.[10,11,33–35] (1) The hierarchical ZCO/NiO NWs possess larger surface areas; therefore, they have an enhanced portion of exposed surfaces, which provide more active sites for Li ion access, to ensure a high utilization of electrode materials.[23,36–38] (2) The novel 3D array architecture with porous textures can provide facile diffusion of the electrolyte/ions and thus shorten the transport pathway of the Li ions to the surface of the active material, resulting in an enhanced rate capability with respect to the pristine ZCO NWs.[16,36,39] In comparison with the pristine ZCO NWs, the highly dense NiO nanosheet coated on the ZCO NWs may relieve the stress exerted on inner nanowires caused by severe volume changes, arising from alloying/dealloying, and thus suppress the degradation of the core ZCO material.[40,41] (3) Compared to the ZCO NWs, the porous nature of the ZCO/NiO NWs between the interior of the ZCO nanowire cores and the exterior of the NiO nanosheet is beneficial for relieving the strain induced by the volume change during cycling, and therefore lead to improved cycling stability.[42–44] (4) The increased electronic conductivity may also be an important factor in improving the electrochemical performance of the electrode materials.[45–48] The higher capacity, improved rate capability and cycling stability of the ZCO/NiO NW composite electrodes indicate the efficiency of our protocol in constructing 3D core/shell nanostructures for improving the electrochemical performance of electrode materials.

Conclusions

In conclusion, we have demonstrated a facile, controllable synthesis of freestanding hierarchical ZCO/NiO NWs on Ni foam by applying a simple, cost-effective hydrothermal growth combined with a subsequent chemical bath deposition method. High-resolution scanning and transmission electron microscopies reveal that the ultra-thin NiO nanosheets uniformly grew on the porous ZnCo$_2$O$_4$ nanowire with many interpartical mesopores, resulting in the formation of 3D core/shell nanowire arrays with hierarchical architecture. The as-prepared arrays were directly used as binders and additive-free anodes for LIBs by using a standard half-cell configuration. The results show that the ZCO/NiO NWs have a higher capacity, improved rate capability and cycling stability with respect to the pristine ZCO NWs, which is mainly attributed to the synergistic contribution between the ZCO nanowire cores and the NiO nanosheet shells, as well as the high surface area and porous-array geometry. It is expected that this synthetic protocol can be further extended to build additional 3D core/shell nanostructures using low-cost and earth-abundant materials for energy storage applications.

Acknowledgements

Notes and references

1 C. Q. Shang, S. M. Dong, S. Wang, D. D. Xiao, P. X. Han, X. G. Wang, L. Gu and G. L. Cui, *ACS Nano*, 2013, **7**, 5430–5436.

2 S. Han, C. Li, Z. Q. Liu, B. Lei, D. H. Zhang, W. Jin, X. L. Liu, T. Tang and C. W. Zhou, *Nano Lett.*, 2004, **4**, 1241–1246.

3 L. Q. Mai, F. Yang, Y. L. Zhao, Q. X. Xu, L. Xu and Y. Z. Luo, *Nat. Commun.*, 2011, **2**, 381.

4 A. S. Aricò, P. Bruce, B. Scrosati, J. M. Tarascon and W. Van Schalkwijk, *Nat. Mater.*, 2005, **4**, 366–377.

5 K. Wang, J. Chen, W. Zhou, Y. Zhang, Y. Yan, J. Pern and A. Mascarenhas, *Adv. Mater.*, 2008, **20**, 3248–3253.

6 W. Li, J. P. Yang, Z. X. Wu, J. X. Wang, B. Li, S. S. Feng, Y. H. Deng, F. Zhang and D. Y. Zhao, *J. Am. Chem. Soc.*, 2012, **134**, 11864–11867.

7 S. M. Dong, X. Chen, L. Gu, X. H. Zhou, L. F. Li, Z. H. Liu, P. X. Han, H. X. Xu, J. H. Yao, H. B. Wang, X. Y. Zhang, C. Q. Shang, G. L. Cui and L. Q. Chen, *Energy Environ. Sci.*, 2013, **4**, 3502–5408.

8 Y. Wu, J. Xiang, C. Yang, W. Lu and C. M. Lieber, *Nature*, 2004, **430**, 61–65.

9 C. W. Cheng, B. Liu, H. Y. Yang, W. W. Zhou, L. Sun, R. Chen, S. F. Yu, J. X. Zhang, H. Gong, H. D. Sun and H. J. Fan, *ACS Nano*, 2009, **3**, 3069–3076.

10 W. W. Zhou, Y. Y. Tay, X. T. Jia, D. Y. Yau Wai, J. Jiang, H. H. Hoon and T. Yu, *Nanoscale*, 2012, **4**, 4459–4463.

11 Y. S. Luo, J. S. Luo, J. Jiang, W. W. Zhou, H. P. Yang, X. Y. Qi, H. Zhang, H. J. Fan, D. Y. W. Yu, C. M. Li and T. Yu, *Energy Environ. Sci.*, 2012, **5**, 6559–6566.

12 W. Q. Zeng, F. P. Zheng, R. Z. Li, Y. Zhan, Y. Y. Li and J. P. Liu, *Nanoscale*, 2012, **4**, 2760–2765.

13 X. H. Xia, J. P. Tu, Y. Q. Zhang, X. L. Wang, C. D. Gu, X. B. Zhao and H. J. Fan, *ACS Nano*, 2012, **6**, 5531–5538.

14 G. R. Li, Z. L. Wang, F. L. Zheng, Y. N. Ou and Y. X. Tong, *J. Mater. Chem.*, 2011, **21**, 4217–4221.

15 X. H. Lu, T. Zhai, X. H. Zhang, Y. Q. Shen, L. Y. Yuan, B. Hu, L. Gong, J. Chen, J. Zhou, Y. X. Tong and Z. L. Wang, *Adv. Mater.*, 2012, **24**, 938–944.

16 J. Yan, A. Sumboja, E. Khoo and P. S. Lee, *Adv. Mater.*, 2011, **23**, 746–750.

17 H. Wang, D. Ma, X. Huang, Y. Huang and X. Zhang, *Sci. Rep.*, 2012, **2**, 701.

18 J. P. Liu, J. Jiang, C. W. Cheng, H. X. Li, J. X. Zhang, H. Gong and H. J. Fan, *Adv. Mater.*, 2011, **23**, 2076–2081.

19 L. Yu, G. Q. Zhang, C. Z. Yuan and X. W. Lou, *Chem. Commun.*, 2013, **49**, 137–139.

20 J. Jiang, Y. Y. Li, J. P. Liu, X. T. Huang, C. Z. Yuan and X. W. Lou, *Adv. Mater.*, 2012, **24**, 5166–5180.

21 B. Liu, J. Zhang, X. F. Wang, G. Chen, D. Chen, C. W. Zhou and G. Z. Shen, *Nano Lett.*, 2012, **12**, 3005–3011.

22 B. Varghese, M. V. Reddy, Z. Yanwu, C. S. Lit, T. C. Hoong, G. V. S. Rao, B. V. R. Chowdari, A. T. Shen Wee, C. T. Lim and C. H. Sow, *Chem. Mater.*, 2008, **20**, 3360–3367.

23 Y. Sharma, N. Sharma, G. V. Subba Rao and B. V. R. Chowdari, *Adv. Funct. Mater.*, 2007, **17**, 2855–2861.

24 W. Luo, X. L. Hu, Y. M. Sun and Y. H. Huang, *J. Mater. Chem.*, 2012, **22**, 8916–8921.

25 Y. C. Qiu, S. H. Yang, H. Deng, L. M. Jin and W. S. Li, *J. Mater. Chem.*, 2010, **20**, 4439–4444.

26 N. Du, Y. F. Xu, H. Zhang, J. X. Yu, C. X. Zhai and D. R. Yang, *Inorg. Chem.*, 2011, **50**, 3320–3324.

27 S. A. Needham, G. X. Wang and H. K. Liu, *J. Power Sources*, 2006, **159**, 254–257.

28 D. Su, M. Ford and G. Wang, *Sci. Rep.*, 2012, **2**, 924.

29 X. H. Xia, J. P. Tu, J. Zhang, X. L. Wang, W. K. Zhang and H. Huang, *Sol. Energy Mater. Sol. Cells*, 2008, **92**, 628–633.

30 N. Mironova-Ulmane, A. Kuzmin, I. Steins, J. Grabis, I. Sildos and M. Pars, *J. Phys.: Conf. Ser.*, 2007, **93**, 012039.

31 K. Samanta, P. Bhattacharya, R. S. Katiyar, W. Iwamoto, P. G. Pagliuso and C. Rettori, *Phys. Rev. B: Condens. Matter Mater. Phys.*, 2006, **73**, 245213.

32 C. C. Ai, M. C. Yin, C. W. Wang and J. T. Sun, *J. Mater. Sci.*, 2004, **39**, 1077–1079.

33 G. F. Ortiz, I. Hanzu, P. Lavela, P. Knauth, J. L. Tirado and T. Djenizian, *Chem. Mater.*, 2010, **22**, 1926–1932.

34 S. L. Xiong, J. S. Chen, X. W. Lou and H. C. Zeng, *Adv. Funct. Mater.*, 2012, **22**, 861–871.

35 W. W. Zhou, J. Zhu, C. W. Cheng, J. P. Liu, H. P. Yang, C. X. Cong, C. Guan, X. T. Jia, H. J. Fan, Q. Y. Yan, C. M. Li and T. Yu, *Energy Environ. Sci.*, 2011, **4**, 4954–4961.

36 P. L. Taberna, S. Mitra, P. Poizot, P. Simon and J. M. Tarascon, *Nat. Mater.*, 2006, **5**, 567–573.

37 Y. Liu, C. H. Mi, L. H. Su and X. G. Zhang, *Electrochim. Acta*, 2008, **53**, 2507–2513.

38 W. W. Zhou, C. W. Cheng, J. P. Liu, Y. Y. Tay, J. Jiang, X. T. Jia, J. Zhang, H. Gong, H. H. Hng, T. Yu and H. J. Fan, *Adv. Funct. Mater.*, 2011, **21**, 2439–2445.

39 Y. N. NuLi, P. Zhang, Z. P. Guo, H. K. Liu and J. Yang, *Electrochem. Solid-State Lett.*, 2008, **11**, A64–A67.

40 X. J. Zhu, Y. W. Zhu, S. Murali, M. D. Stoller and R. S. Ruoff, *ACS Nano*, 2011, **5**, 3333–3338.

41 Y. G. Li, B. Tan and Y. Y. Wu, *Nano Lett.*, 2008, **8**, 265–270.

42 Y. Wang, H. C. Zeng and J. Y. Lee, *Adv. Mater.*, 2006, **18**, 645–649.

43 Y. Wang, H. Xia, L. Lu and J. Y. Lin, *ACS Nano*, 2010, **4**, 1425–1432.

44 Y. Wang and G. Z. Cao, *Adv. Mater.*, 2008, **20**, 2251–2269.

45 W. Ai, L. H. Xie, Z. Z. Du, Z. Y. Zeng, J. Q. Liu, H. Zhang, Y. H. Huang, W. Huang and T. Yu, *Sci. Rep.*, 2013, **3**, 2341.

46 J. S. Chen, C. M. Li, W. W. Zhou, Q. Y. Yan, L. A. Archer and X. W. Lou, *Nanoscale*, 2009, **1**, 280–285.

47 J. F. Li, J. Z. Wang, D. Wexler, D. Q. Shi, J. W. Liang, H. K. Liu, S. L. Xiong and Y. T. Qian, *J. Mater. Chem. A*, 2013, **1**, 15292–15299.

48 W. Ai, Z. Z. Du, Z. X. Fan, J. Jiang, Y. L. Wang, H. Zhang, L. H. Xie, W. Huang and T. Yu, *Carbon*, 2014, DOI: 10.1016/j.carbon.2014.04.061.